


Hyperscaling in the Coherent Hyperspin Machine

Marcello Calvanese Strinati^{1,*} and Claudio Conti^{2,1}

¹*Centro Ricerche Enrico Fermi (CREF), Via Panisperna 89a, 00184 Rome, Italy*

²*Physics Department, Sapienza University of Rome, 00185 Rome, Italy*

 (Received 4 August 2023; revised 6 November 2023; accepted 6 December 2023; published 3 January 2024)

Classical and quantum systems are used to simulate the Ising Hamiltonian, an essential component in large-scale optimization and machine learning. However, as the system size increases, devices like quantum annealers and coherent Ising machines face an exponential drop in their success rate. Here, we introduce a novel approach involving high-dimensional embeddings of the Ising Hamiltonian and a technique called “dimensional annealing” to counteract the decrease in performance. This approach leads to an exponential improvement in the success rate and other performance metrics, slowing down the decline in performance as the system size grows. A thorough examination of convergence dynamics in high-performance computing validates the new methodology. Additionally, we suggest practical implementations using technologies like coherent Ising machines, all-optical systems, and hybrid digital systems. The proposed hyperscaling heuristics can also be applied to other quantum or classical Ising devices by adjusting parameters such as nonlinear gain, loss, and nonlocal couplings.

DOI: [10.1103/PhysRevLett.132.017301](https://doi.org/10.1103/PhysRevLett.132.017301)

Hard optimization problems permeate science and society and are crucial to machine learning [1], traffic and portfolio optimization [2], markets and finance [3], life science [4], bioinformatics [5], protein folding [6], and epidemic spreading [7]. Finding efficient ways to tackle such problems means determining the optimal configuration of a massive amount of degrees of freedom interacting in a highly nontrivial way. Building a generation of computing machines to tackle large-scale optimization is one of the most significant challenges of modern science.

A viable route is offered by the possibility of mapping optimization problems onto a classical Ising Hamiltonian [8]. Solving the problem translates into finding the ground state (GS) of the corresponding Ising system. Quantum annealers (QAs) as D-Wave achieve this mapping by superconducting technology [9,10]. The last QA’s generation reaches the scale of 5000 qubits [11]. Coherent Ising machines (CIMs) [12] exploit optical pulses in a network of degenerate parametric oscillators (POs) simulating up to 100 000 spins with tunable couplings [13].

Both of these groundbreaking technologies suffer poor scaling with the number of spins N . The success probability drops more than exponentially with N for QAs, while a better performance has been reported for the CIMs [14]. When N grows, the number of local minima grows exponentially for a spin glass. Correspondingly, the probability of being stuck in a suboptimal solution increases. This mechanism lies at the origin of the poor scaling of Ising machines and optimization algorithms.

During a run in an annealing device, one carefully chooses specific hyperparameters as the pump power h of CIMs. A large number of local minima narrows the range

of h where the GS is found [15]. The difference between the final energy E after minimization and the target GS energy E_{GS} signals the absence of convergence. A strategy to overcome these detrimental effects is increasing dimensionality, for example, by replacing the binary Ising model with continuous spin systems. Considering one local minimum in the phase space, additional dimensions turn the minimum into a saddle and open escape directions. However, this also affects the global minimum, whose energy lowers when the number of dimensions increases. By increasing the dimensionality, one escapes local minima but loses the opportunity to identify the target (Ising) GS.

We introduced the idea of hyperspins and dimensional annealing to exploit large dimensional spaces [16]. One starts from the binary Ising model encoding a graph defined by a coupling matrix \mathbf{J}_N . The binary spins are replaced by unitary vectors in a D -dimensional space (the *hyperspins*) on a hypergraph with the same \mathbf{J}_N . The hyperspin time evolution leads to a steady-state energy $E < E_{GS}$. After reaching the steady state, the topology of the hypergraph morphs adiabatically to the original binary Ising model, a heuristic that we name *dimensional annealing*. Notably, the approach radically widens the parameter range of successful convergence to the Ising GS for dense and computationally hard graphs [16].

However, the way to physically realize hyperspins and dimensional annealing has yet to be considered. The literature has reported proposals relying on nonlinear POs [17,18] and the first observation of hyperspin dynamics [19]. In this Letter, we discuss different implementations of the hyperspin machine and validate the resulting coherent hyperspin machine (CHYM) by first-principle

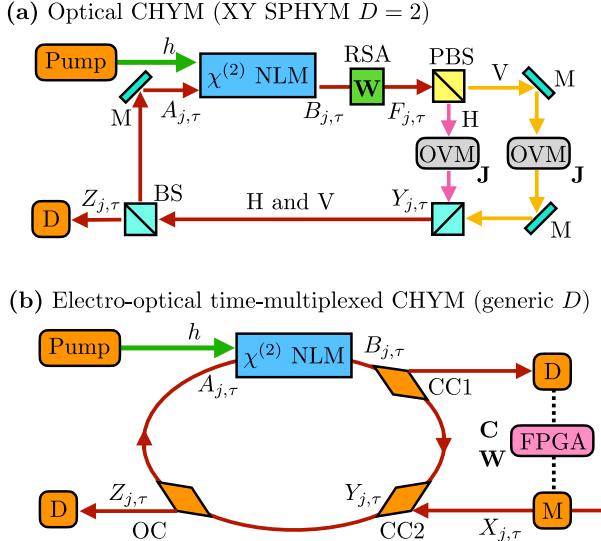


FIG. 1. CHYM designs. (a) All-optical spatial CHYM (SPHYM) with $D=2$. The N hyperspins are encoded as different spatial points on the signal optical wave front [22], and the $D=2$ components are the two polarizations H and V at each point. The scheme comprises $\chi^{(2)}$ nonlinear medium (NLM) pumped by a field at amplitude h , reverse saturable absorber (RSA) implementing \mathbf{W} , polarizing beam splitter (PBS), optical vector matrix multipliers (OVMs) implementing \mathbf{J}_N , and beam splitters (BS) for recombinations and extraction to the detector (D). (b) Hybrid CHYM with generic D . POs are generated optically by a $\chi^{(2)}$ NLM as a train of DN spatially separated pulses [23]. The blocks are couplers (CC1 and CC2) connecting the cavity to the electronic feedback, detector (D), FPGA implementing \mathbf{W} and \mathbf{C} , modulator (M), output coupler (OC), and detector (D). The fields $A_{j,\tau}$, $B_{j,\tau}$, $F_{j,\tau}$, $X_{j,\tau}$, $Y_{j,\tau}$, and $Z_{j,\tau}$ after the respective blocks are shown.

parallel large-scale simulations. We also compare with the XY machine [20,21]. We show an exponential increase in the probability of success, with one order of magnitude improvement in the convergence range and accuracy of the GS energy.

Two implementations of the hyperspin machine are shown in Fig. 1: Fig. 1(a), the all-optical, following [17], designed for the XY model ($D=2$), and Fig. 1(b), hybrid (electro-optical), based on [14,23–25], for generic D . Compared to the Ising machine, the hyperspin machine introduces a nonlinear coupling involving D POs at once, effectively turning a system of DN linearly and nonlinearly coupled POs into a network of N , D -dimensional hyperspins [16]. In Fig. 1(a), the N hyperspins are encoded in different spatial points on the signal wave front [22], and the $D=2$ components are the two polarizations H and V at each point.

A $\chi^{(2)}$ nonlinear medium (NLM), pumped by a field at amplitude h and frequency $2\omega_0$, amplifies the PO fields at frequency ω_0 , enforcing a phase 0 or π with respect to the pump ($A_{j,\tau}$ is real [17]). Here $j=1, \dots, DN$ labels the POs

and $\tau=1, \dots, \tau_{\max}$ counts the cavity round-trip. The NLM transforms $A_{j,\tau}$ into $B_{j,\tau}$. The nonlinear coupling by the matrix \mathbf{W} is induced by a reverse saturable absorber (RSA), which reduces the amplitude of each hyperspin by its intensity, yielding $F_{j,\tau}$.

A polarizing beam splitter (PBS) spatially separates H and V . Two optical vector matrix multipliers (OVMs) implement the coupling including self-interaction and the matrix \mathbf{J}_N [17]. The recombined polarizations yield $Y_{j,\tau} = \sum_{l=1}^{DN} Q_{jl} F_{l,\tau}$, where $\mathbf{Q} = a\mathbb{1}_{DN} + b\mathbf{C}$, with $a+b=1$ and $\mathbf{C} = \mathbf{J}_N \otimes \mathbb{1}_D$ is the linear coupling matrix implementing the Euclidian scalar product between hyperspins [16]. Then, $Z_{j,\tau} = dY_{j,\tau}$ with $d < 1$ is extracted by a beam splitter (BS), so $A_{j,\tau+1} = (1-d)Y_{j,\tau}$ is the field at the subsequent round-trip. This recurrence relation allows us to describe the CHYM dynamics by a discrete-time nonlinear map [26] (see [15,17,27] for studies on Ising machines).

Figure 1(b) shows the electro-optical hyperspin machine based on [14,23,24], where the DN POs are spatially separated optical pulses. The electronic coupling device composed by identical couplers (CC1 and CC2), field programmable gate array (FPGA), detector (D), and modulator (M), arranges the DN POs as N , D -dimensional hyperspins and couples them. CC1 extracts a fraction of the amplified fields $B_{j,\tau}$. The FPGA preprogrammed with \mathbf{W} and \mathbf{C} computes the feedback fields $X_{j,\tau}$, which modulate the optical field injected into the cavity, yielding $Y_{j,\tau}$ after CC2. Detection occurs at the output coupler (OC); see Supplemental Material (SM) for details [28].

Another hybrid scheme was proposed in [29], where the coupling is implemented optically by OVM [17,30], while the nonlinearity is electronically computed. All-optical machines potentially offer the largest speedup over digital electronics [the setup in Fig. 1(a) is expected to perform ultrafast, size-independent computation [17,22]], but their implementation is currently a major challenge. Instead, existing hybrid setups allow the implementation of the hyperspin machine in a fully controllable way by simple software modifications. Hence, we analyze the scaling performance of the hyperspin machine focusing on Fig. 1(b) (other schemes are discussed in the SM [28]).

Figure 2 shows the CHYM working principle, with the dynamics of the hyperspin energy E_{hs} (see SM) for (I) CHYM (simulating the XY model [31] with $D=2$, blue line), (II) CHYM with dimensional annealing (interpolating between $D=2$ and $D=1$, red line), and (III) CIM ($D=1$, orange line). During the dynamics, the system explores different spin configurations behaving as gradient descent in the energy landscape of the coupled POs [16]. For Ising machines (orange line), whose energy landscape is sketched in Fig. 2(a) as the black wavy line, spins undergo discrete flips, exploring local minima at decreasing energy that may trap the system, preventing the reach of the Ising GS. Instead, the CHYM converges to an energy below the Ising GS (blue line). Remarkably, since Ising states are

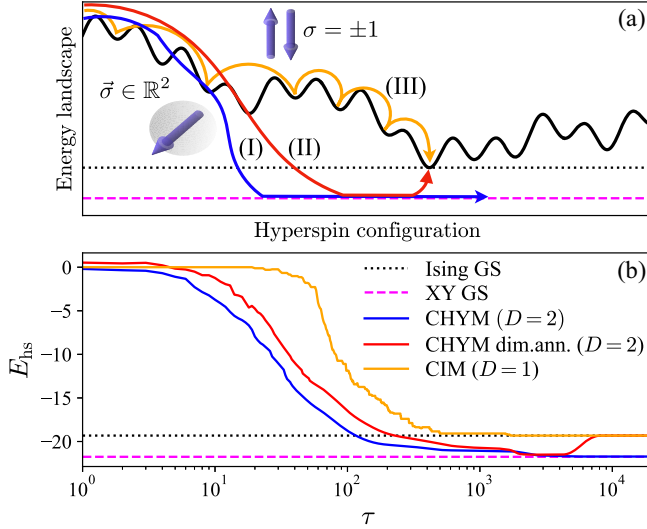


FIG. 2. (a) Sketch of energy dynamics on the Ising energy landscape showing the principle of operation of the CHYM working as (I) *XY* machine ($D = 2$, blue line), (II) *XY* machine with dimensional annealing (from $D = 2$ to $D = 1$, red line), and (III) Ising machine ($D = 1$, orange line). Full black wavy line depicts the Ising energy landscape for the CIM. Horizontal dotted black and dashed magenta line mark the minimum (GS) energies for the Ising and *XY* model, respectively. The CIM approaches the Ising GS from larger energy values, visiting local minima by flipping the Ising spins $\sigma = \pm 1$ (arrows) during the evolution that can trap the dynamics. On the contrary, the CHYM simulates continuous spins $\vec{\sigma} \in \mathbb{R}^2$ (arrow in the sphere) and is insensitive to the Ising local minima. The energy tunnels straight toward the *XY* GS, which is below the Ising GS. From the *XY* GS, the Ising GS energy is approached from below by the dimensional annealing. (b) Hyperspin energy E_{hs} during the round-trips τ from a CHYM simulation, confirming the picture in (a).

not fixed points of the hyperspin dynamics, the hyperspins evolve towards their GS and cannot be trapped in Ising local minima. When dimensional annealing is performed from the hyperspin GS, the Ising GS is approached from below (red line). The combined effect of being insensitive to Ising local minima and approaching the Ising GS from below is at the core of the enhanced performance of the CHYM with dimensional annealing, as detailed hereafter.

We use the map for the numerical simulation of the CHYM and validate the picture in Fig. 2(b) for $N = 100$. We focus on \mathbf{J}_N describing random binary sparse graphs with density 20%. Dimensional annealing is implemented on \mathbf{C} as detailed in the SM [28].

The CHYM has two sources of nonlinearity: the $\chi^{(2)}$ NLM (local, with strength κL being L the propagation length) and the FPGA (nonlocal, with strength βb^2). Previous studies argued that local nonlinearities are crucial to the functioning of Ising machines, while nonlocal nonlinearities are detrimental [15,19]. Instead, the hyperspin machine works with only nonlocal nonlinearities [16]. Therefore, we set (I) $\kappa L = 10^{-3}$ for the CHYM, (II)

$\kappa L = 10^{-1}$ for the CHYM with dimensional annealing, with $\beta b^2 = 25$ in both cases to have a dominating FPGA nonlinearity, and (III) $\kappa L = 10^{-1}$ and $\beta = 0$ for the CIM.

In Fig. 2(b), we see that (I) the CHYM rapidly converges to the *XY* GS energy (relative deviation below 0.14%), (II) the CHYM with dimensional annealing first converges close to the *XY* GS and then to the Ising GS from lower energy, and (III) the CHYM used as a CIM converges to the Ising GS from above [32]. These results are in agreement with [16], demonstrating that the CHYM in Fig. 1 as an implementation of the hyperspin machine.

The remarkable outcome is that existing hybrid implementations of CIMs can be adapted into CHYMs by a software modification, which enables us to simulate general continuous spin models and novel annealing strategies using off-the-shelf experimental setups.

We now move to the statistical and scaling analysis of the performance comparison of the CHYM working as a CIM and as an *XY* machine with dimensional annealing. The performance is quantified by running for fixed parameters the CHYM map N_r times and computing at the steady state two quantities: the success probability P_{Ising} and the histogram H_E of energy levels. Here, P_{Ising} counts the fraction of the N_r repetitions in which the CHYM converges to the Ising GS energy E_{GS} . Instead, H_E is the number of times a given Ising energy E is found.

Previous work reported on the strong dependency of P_{Ising} on both system parameters and coupling matrix [14–16]. To have a reliable statistics, we simulate the dynamics for $N_g = 100$ sparse graphs with $\tau_{\text{max}} = 15 \times 10^4$, and for N ranging from 10 to 100. We repeat the simulations for N_s values of the pump amplitude $h = h_{\text{th}}(1 + \delta h)$ by scanning the relative deviation δh from threshold h_{th} . We have $N_s = 51, 21$ for $D = 1, 2$, respectively, and $N_r = 100$.

Figure 3 exemplifies the behavior of $P_{\text{Ising}}(h)$ and H_E . By comparing $D = 1$ (blue) and $D = 2$ (red), we observe three striking differences: (i) P_{Ising} for $D = 2$ has higher maximum value over the pump scans, (ii) P_{Ising} for $D = 2$ has a much weaker dependency on h , and (iii) H_E is considerably closer to E_{GS} . The dimensional annealing boosts the performance of the CHYM in terms of enhanced accuracy in the Ising GS and reduced sensitivity to the system hyperparameters.

The analysis suggests three figures of merit from Fig. 3: $P_{\text{Ising,max}}$ giving the maximum value of $P_{\text{Ising}}(h)$, W quantifying $P_{\text{Ising}}(h)$ and its sensitivity on h , and $\Delta E = \sum_E (E - E_{\text{GS}}) H_E$ giving the average energy deviation from the GS (see SM [28]). Figure 4 shows the finite-size scaling of $\bar{P}_{\text{Ising,max}}$, \bar{W} , and $\bar{\Delta E}$, defined, respectively, as the averages of $P_{\text{Ising,max}}$, W , and ΔE , over the N_g graphs. Data are shown as connected points (blue and red for $D = 1, 2$, respectively). The uncertainty is the interquartile range (IQR, shaded areas).

The decay $\bar{P}_{\text{Ising,max}}$ in Fig. 4(a) is well captured by an exponential $\sim e^{-a_d N}$ in both cases (orange and green dashed

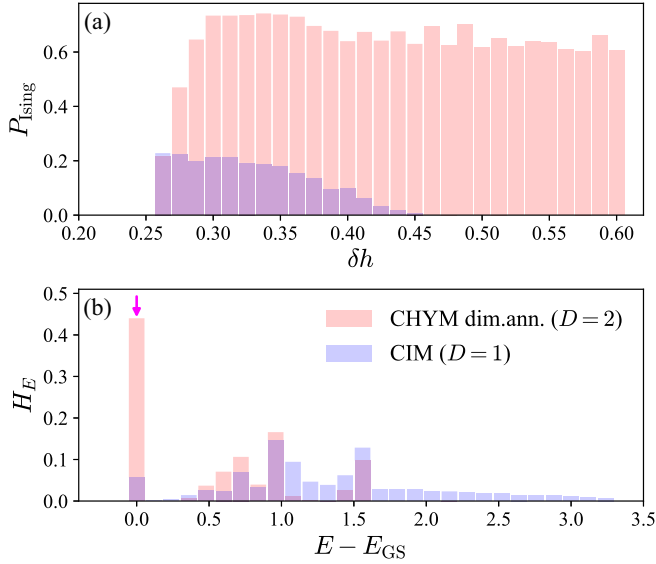


FIG. 3. Typical distribution of (a) success probability to solve the Ising model P_{Ising} as a function of δh and (b) histogram H_E of energy levels as a function of $E - E_{\text{GS}}$, comparing the data from the CIM (blue) and those from the CHYM with dimensional annealing (red). The magenta arrow marks the GS value $E = E_{\text{GS}}$. Compared to the CIM, the CHYM with dimensional annealing provides (i) P_{Ising} almost independent of δh (where nonzero) and with higher maximum value, and (ii) higher probability H_E to converge to low-energy Ising states. Data are shown for a random graph with $N = 100$ for illustration purposes (SM reports comprehensive results [28]).

lines), with $a_1/a_2 \simeq 2.32$. For $D = 1$, this exponential trend agrees with Ref. [14]. The implication of this result is twofold: First, the decay of $\bar{P}_{\text{Ising,max}}$ for the CHYM with dimensional annealing is also exponential, and second, its decay rate is halved compared to the CIM. In other words, the CHYM with dimensional annealing shows a decay of $\bar{P}_{\text{Ising,max}}$ that is exponentially slower (i.e., the performance is exponentially improved) by a factor $e^{(a_1 - a_2)N}$.

The scaling of $\bar{P}_{\text{Ising,max}}$ is complemented by \bar{W} in Fig. 4(b), which gives comprehensive information on the dependence on h of the success rate. We see that \bar{W} for $D = 2$ is almost one order of magnitude larger than for $D = 1$. The dimensional annealing makes on average $P_{\text{Ising}}(h)$ significantly less sensitive to the specific value of h . Remarkably, this implies that the CHYM with dimensional annealing does not require a fine calibration of the pump to operate in the optimal regime. We ascribed the large IQR to the strong graph dependency of the considered figures of merit.

Figure 4(c) shows $\overline{\Delta E}$. As evident, $\overline{\Delta E}$ for $D = 1$ starts from ~ 0.1 at $N = 10$, and rapidly increases with N reaching ~ 1.0 for $N = 100$. Instead, for $D = 2$, $\overline{\Delta E}$ is close to zero up to $N = 60$, showing a slower increase compared to $D = 1$, reaching ~ 0.1 at $N = 100$. The reported data provide clear

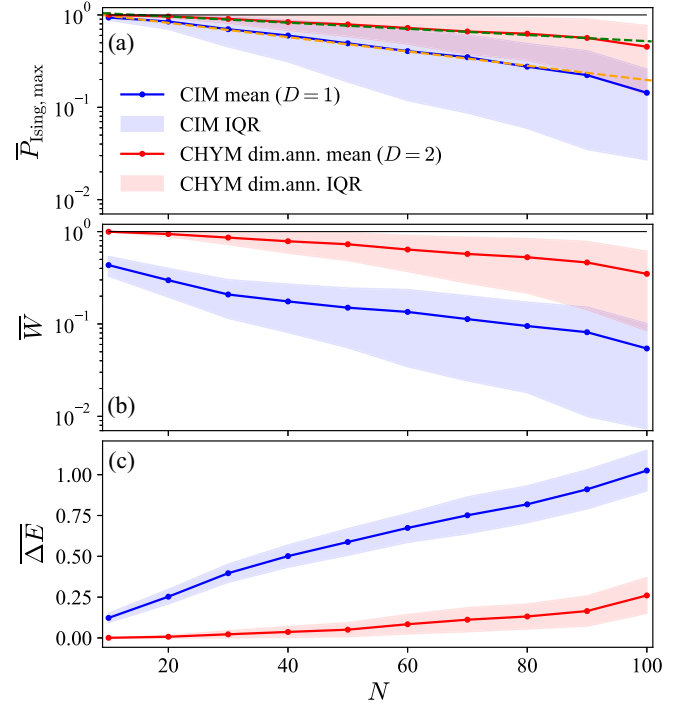


FIG. 4. Finite-size scaling of (a) $\bar{P}_{\text{Ising,max}}$, (b) \bar{W} , and (c) $\overline{\Delta E}$, statistically quantifying the advantages of the CHYM with dimensional annealing over the CIM: (i) higher probability to solve the Ising model, (ii) reduced dependency on the pump amplitude, and (iii) enhanced convergence to low-energy Ising states (see also Fig. 3). Mean value (points) and IQR (shaded areas) are computed by averaging over $N_g = 100$ graphs for each value of N and D (see text). Dashed lines in top panel are exponential functions $f_D(N) = b_D e^{-a_D N}$, with $a_1 \simeq 18 \times 10^{-3}$ (orange dashed line) and $a_2 \simeq 8 \times 10^{-3}$ (green dashed line). Notice the log-linear scale in (a) and (b).

evidence that the CHYM increases the tendency to converge to low-energy Ising states.

In conclusion, an extensive statistical analysis shows that the hyperspin heuristics enhances the finite-size scaling of Ising machines. We identified three figures of merit: (i) maximum success rate, (ii) sensitivity of the success rate to pump amplitude, and (iii) convergence accuracy to the Ising GS. High-performance-computing simulations furnish the scaling of the figures of merit averaged over hundreds of graphs. The dimensional annealing exponentially improves the figures of merit in the accuracy of the optimal solution and also in the sensitivity to hyperparameters. The approach can be combined with other algorithms [33], where scaling advantages were also reported, as it will be detailed in the future.

Here we used dimensional annealing from $D = 2$ to $D = 1$. An intriguing perspective is whether annealing from $D > 2$ further enhances the performance, or if performance saturation occurs.

Also, a simple software modification to the CIM feedback mechanism enables an experimental implementation

through an effective nonlinear coupling between POs. For a family of random graphs, we unveiled that the resulting CHYM can handle general high-dimensional models and dimensional annealing. Compared with the CIM, the CHYM has a more reliable and successful convergence to the Ising GS and does not require a fine calibration of the pump amplitude. Our proposal turns state-of-the-art CIMs into hyperspin machines boosting their performance.

The application of hyperspins and dimensional annealing extends to many software and hardware platforms, including nonlinear optics, quantum devices, and dedicated digital electronics. The crucial recipe is engineering the nonlocal couplings and the nonlinear loss. The high-dimensional embedding not only may accelerate by orders of magnitude classical and quantum computing, but also trigger the development of new algorithms for large-scale optimization and machine learning.

We acknowledge the CINECA award under the IS CRA initiative for the availability of high-performance-computing resources and support. Numerical simulations of the CHYM are performed using a dedicated C-language code exploiting multiprocessing on the CINECA GALILEO100 supercomputer over 400 CPUs. C. C. acknowledges financial support from CN1 Quantum PNRR MUR CN_0000013 HPC.

* marcello.calvanesestrinati@gmail.com

- [1] P. Date, D. Arthur, and L. Pusey-Nazzaro, QUBO formulations for training machine learning models, *Sci. Rep.* **11**, 10029 (2021).
- [2] D. I. Graham and M. J. Craven, An exact algorithm for small-cardinality constrained portfolio optimisation, *J. Oper. Res. Soc.* **72**, 1415 (2021).
- [3] B. Hemenway and S. Khanna, Sensitivity and computational complexity in financial networks, *Algorithmic Finance* **5**, 95 (2017).
- [4] Q. Zhang, D. Deng, W. Dai, J. Li, and X. Jin, Optimization of culture conditions for differentiation of melon based on artificial neural network and genetic algorithm, *Sci. Rep.* **10**, 3524 (2020).
- [5] A. Degasperi, D. Fey, and B. N. Kholodenko, Performance of objective functions and optimisation procedures for parameter estimation in system biology models, *npj Syst. Biol. Appl.* **3**, 20 (2017).
- [6] N. A. Pierce and E. Winfree, Protein design is NP-hard, *Protein Eng.* **15**, 779 (2002).
- [7] C. H. Cheng, Y. H. Kuo, and Z. Zhou, Outbreak minimization vs influence maximization: An optimization framework, *BMC Med. Inform. Decis. Mak.* **20**, 266 (2020).
- [8] A. Lucas, Ising formulations of many NP problems, *Front. Phys.* **2**, 5 (2014).
- [9] R. Harris *et al.*, Phase transitions in a programmable quantum spin glass simulator, *Science* **361**, 162 (2018).
- [10] A. D. King *et al.*, Coherent quantum annealing in a programmable 2,000 qubit Ising chain, *Nat. Phys.* **18**, 1324 (2022).
- [11] A. D. King *et al.*, Quantum critical dynamics in a 5,000-qubit programmable spin glass, *Nature (London)* **617**, 61 (2023).
- [12] P. L. McMahon, A. Marandi, Y. Haribara, R. Hamerly, C. Langrock, S. Tamate, T. Inagaki, H. Takesue, S. Utsunomiya, K. Aihara, R. L. Byer, M. M. Fejer, H. Mabuchi, and Y. Yamamoto, A fully programmable 100-spin coherent Ising machine with all-to-all connections, *Science* **354**, 614 (2016).
- [13] T. Honjo, T. Sonobe, K. Inaba, T. Inagaki, T. Ikuta, Y. Yamada, T. Kazama, K. Enbutsu, T. Umeki, R. Kasahara, K. Kawarabayashi, and H. Takesue, 100,000-spin coherent Ising machine, *Sci. Adv.* **7**, eabh0952 (2021).
- [14] R. Hamerly *et al.*, Experimental investigation of performance differences between coherent Ising machines and a quantum annealer, *Sci. Adv.* **5**, eaau0823 (2019).
- [15] M. Calvanese Strinati, L. Bello, E. G. Dalla Torre, and A. Pe'er, Can nonlinear parametric oscillators solve random Ising models?, *Phys. Rev. Lett.* **126**, 143901 (2021).
- [16] M. Calvanese Strinati and C. Conti, Multidimensional hyperspin machine, *Nat. Commun.* **13**, 7248 (2022).
- [17] M. Calvanese Strinati, D. Pierangeli, and C. Conti, All-optical scalable spatial coherent Ising machine, *Phys. Rev. Appl.* **16**, 054022 (2021).
- [18] Y. Yonezu, K. Inaba, Y. Yamada, T. Ikuta, T. Inagaki, T. Honjo, and T. Takesue, 10-GHz-clock time-multiplexed non-degenerate optical parametric oscillator network with a variable planar lightwave circuit interferometer, *Opt. Lett.* **48**, 5787 (2023).
- [19] S. Ben-Ami, I. Aharonovich, and A. Pe'er, Persistent dynamics in coupled non-degenerate parametric oscillators: Pump saturation prevents mode competition, *Opt. Express* **31**, 9264 (2023).
- [20] N. G. Berloff, M. Silva, K. Kalinin, A. Askitopoulos, J. D. Töpfer, P. Cilibrizzi, W. Langbein, and P. G. Lagoudakis, Realizing the classical XY Hamiltonian in polariton simulators, *Nat. Mater.* **16**, 1120 (2017).
- [21] I. Gershenzon, G. Arwas, S. Gadasi, C. Tradonsky, A. Friesem, O. Raz, and N. Davidson, Exact mapping between a laser network loss rate and the classical XY Hamiltonian by laser loss control, *Nanophotonics* **9**, 4117 (2020).
- [22] D. Pierangeli, G. Marcucci, and C. Conti, Large-scale photonic Ising machine by spatial light modulation, *Phys. Rev. Lett.* **122**, 213902 (2019).
- [23] H. Takesue, Y. Yamada, K. Inaba, T. Ikuta, Y. Yonezu, T. Inagaki, T. Honjo, T. Kazama, K. Enbutsu, T. Umeki, and R. Kasahara, Observing a phase transition in a coherent Ising machine, *Phys. Rev. Appl.* **19**, L031001 (2023).
- [24] F. Böhm, G. Verschaffelt, and G. Van der Sande, A poor man's coherent Ising machine based on opto-electronic feedback systems for solving optimization problems, *Nat. Commun.* **10**, 3538 (2019).
- [25] H. Takesue, K. Inaba, T. Inagaki, T. Ikuta, Y. Yamada, T. Honjo, T. Kazama, K. Enbutsu, T. Umeki, and R. Kasahara, Simulating Ising spins in external magnetic fields with a network of degenerate optical parametric oscillators, *Phys. Rev. Appl.* **13**, 054059 (2020).
- [26] S. H. Strogatz, *Nonlinear Dynamics and Chaos*, Studies in Nonlinearity (Perseus Books, Reading, PA, 2007).

- [27] M. Calvanese Strinati, I. Aharonovich, S. Ben-Ami, E. G. Dalla Torre, L. Bello, and A. Pe'er, Coherent dynamics in frustrated coupled parametric oscillators, *New J. Phys.* **22**, 085005 (2020).
- [28] See Supplemental Material at <http://link.aps.org/supplemental/10.1103/PhysRevLett.132.017301> for details on the analytical model and additional numerical results.
- [29] K. P. Kalinin, G. Mourgias-Alexandris, H. Ballani, N. G. Berloff, J. H. Clegg, D. Cletheroe, C. Gkantsidis, I. Haller, V. Lyutsarev, F. Parmigiani, L. Pickup, and A. Rowstron, Analog iterative machine (AIM): Using light to solve quadratic optimization problems with mixed variables, [arXiv:2304.12594](https://arxiv.org/abs/2304.12594).
- [30] J. Spall, X. Guo, T. D. Barrett, and A. I. Lvovsky, Fully reconfigurable coherent optical vector–matrix multiplication, *Opt. Lett.* **45**, 5752 (2020).
- [31] H. E. Stanley, Dependence of critical properties on dimensionality of spins, *Phys. Rev. Lett.* **20**, 589 (1968).
- [32] Ising and XY GS energies are found by using a Monte Carlo algorithm and `PYTHON scipy.optimize differential_evolution` minimizer, respectively.
- [33] T. Leleu, F. Khoystatee, T. Levi, R. Hamerly, T. Kohno, and K. Aihara, Scaling advantage of chaotic amplitude control for high-performance combinatorial optimization, *Commun. Phys.* **4**, 266 (2021).